Magnetic force microscopy and nanoindentation on 3D printed magnetic scaffolds for neuronal cell growth

Alex C. Alavarse†, Rafael L. C. G. da Silva†, Pejman Ghaffari Bohlouli‡, Daniel Cornejo††, Henning Ulrich†††, Amin Shavandi‡*, Denise F. S. Petri†*

† Department of Fundamental Chemistry, Institute of Chemistry, University of São Paulo, Av. Prof. Lineu Prestes 748, 05508-000, São Paulo, Brazil; *corresponding author: dfsp@iq.usp.br

†† Institute of Physics, University of São Paulo, 05508-090 São Paulo, Brazil

††† Department of Biochemistry, Institute of Chemistry, University of São Paulo, Av. Prof. Lineu Prestes 748, 05508-000, São Paulo, Brazil

‡ Université Libre de Bruxelles (ULB), Ecole polytechnique de Bruxelles, 3BIO-BioMatter, Avenue F.D. Roosevelt, 50—CP 165/61, 1050, Brussels, Belgium; *corresponding author: amin.shavandi@ulb.be

KEYWORDS: Hydrogels, Printability, Poly(vinyl alcohol), Alginate, Magnetite, Magnetic force microscopy

ABSTRACT: This study investigated the physicochemical properties of 3D printed sodium alginate (SA)/poly(vinyl alcohol) (PVA)-magnetic nanoparticles (MNPs) hydrogels that were subsequently crosslinked using Ca^{2+} ions via post-spraying. The rheological properties of the precursor hydrogels were assessed because they play a crucial role in printability. The SA/PVA composition of 12/8 wt%, both in the absence and presence of MNPs at concentrations of 1.0 mg/mL, 2.5 mg/mL, or 5.0 mg/mL, displayed good printability. Magnetic force microscopy (MFM) evidenced the random distribution of MNPs on the hydrogel surface, and the aggregation of magnetic clusters with increasing MNP content. Nanoindentation tests using a silica colloidal probe allowed estimating the elastic modulus values of swollen 3D printed scaffolds. These values ranged from 1.0 MPa (SA12/PVA8) to 7.2 MPa (SA/PVA-MNP5). Confocal microscopy confirmed the presence of cells within the interior of the 3D printed scaffolds. The cytocompatibility or cytotoxicity assays showed that all 3D printed scaffolds were cytocompatible with HT-22 cells.

1. INTRODUCTION

The advent of 3D printing has ushered in progressive fabrication, enabling the precise and customizable production of complex three-dimensional structures. In the field of biomedicine, the ability to engineer complex geometries and functional designs is of paramount importance for the development of advanced biomedical devices, including tissue scaffolds,[1,2] drug delivery systems,[3] and implantable constructs.[2] Hydrogels, which consist of three-dimensional networks of crosslinked hydrophilic polymers, have emerged as promising bioink materials for 3D printing due to their high biocompatibility, [4,5] tunable mechanical properties,[6] and ability to conjugate bioactive molecules.[7–9] The integration of magnetic nanoparticles (MNPs) into 3D printing for biomedical devices holds great promise and presents exciting prospects.[10,11] By incorporating MNPs, printed constructs gain responsive behavior under external magnetic field (EMF), enabling applications such as targeted drug delivery, [12,13] tissue engineering,[14–16] cancer therapy [17,18] and magnetic resonance imaging.[19]

For tissue engineering, the incorporation of MNPs into scaffolds can provide significant advantages by bringing about favorable changes in the mechanical properties of the system.[20] The development of polymer-MNP composites has demonstrated improvements in *in vitro* cell adhesion, proliferation and differentiation.[21] Hydrogels containing sodium alginate and MNP could guide and promote the growth of Schwann cells, indicating a potential application for peripheral nerve injury repair.[22] Implants based on magnetic alginate, hyaluronic acid and collagen hydrogels promoted the regeneration of axon densities similar to a rat sciatic nerve.[23] Magnetic poly (lactic-co-glycolic acid)

nanofibers successfully differentiated mesenchymal stem cells into neurons. [24] Chitosan-MNP composites mediated the differentiation of neural stem cell (NSC) into neuron during nerve repair. [25] This enhancement is attributed to the inclusion of MNPs, which finely adjust the physicochemical properties of the material. This adjustment includes the modulation of pore size and interconnectivity, ultimately establishing an optimal environment for cell development.[26] In addition, the mechanical properties (stress/strain, elasticity/stiffness) of the scaffolds affect the cell behaviors and signaling pathways.[27,28]

In this context the inclusion of metallic material results in composites characterized by increased stiffness, or even dynamic modifiability through the influence of an external magnetic field. This phenomenon was observed in MNPs embedded in gelatin nanofibers,24 where the application of an external magnetic field induces fiber alignment, thereby enhancing the material's stiffness. In the presence of these aligned fibers, stem cells (ADSC cells) underwent differentiation into osteocytes, whereas in the absence of fiber alignment, the cells differentiated into adipocytes..[29]

Nevertheless, the determined values of mechanical properties can vary depending on the method used. For example, macroscopic compression tests yield the bulk mechanical properties of the material. On the other hand, nanoindentation is a valuable tool for assessing the mechanical properties of scaffolds at a scale closer to that perceived by cells. Atomic force microscopy (AFM) and similar nano-indenter devices are ideally suited for micro-scale measurements because these instruments utilize a precisely defined indenting tip to deform the substrate and measure the requisite force.[27,30] AFM nanoindentation is capable of investigating a wide range of elastic moduli, ranging from relatively low values of 1 kPa to as high as 100 GPa.[31] In this context, AFM-based nanoindentation has provided accurate insights into the mechanical properties of soft materials such as hydrogels,[32] elastomers[33], and biological molecules.[34]

Sodium alginate (SA), a natural polysaccharide derived from brown algae, has gained significant attention and found wide applications in the field of 3D printing for biomedical devices.[35] Its properties make it an ideal bioink material for fabricating complex structures with excellent printability and biocompatibility.[36] Moreover, after printing, the SA structure can be stabilized by the addition of divalent cations such as Ca^{2+}, because the hydrophilic L-guluronic acid (G) units interact instantaneously with divalent cations.[37] The viscosity and gelation behavior of SA can be precisely controlled by adjusting parameters such as alginate concentration and crosslinking agents.[38–41] Mixtures of SA and methylcellulose (MC) were 3D printed into a CaCl2 solution; among many factors, the authors observed that storing the samples in a CaCl2 solution led to increased stiffness due to the diffusion of Ca2+ ions from the medium to the polymer matrix [42]. Furthermore, the biodegradation allows a gradual integration and remodeling of the regenerated tissue, which eliminates the need for invasive removal procedures and reduces potential complications.[43] Poly(vinyl alcohol) (PVA) is a water soluble polymer[44,45] that could enhance the printability of scaffolds in 3D printing.[46,47] SA and PVA are miscible over a broad range of composition,[48] probably due to hydrogen bonding between hydroxyl groups belonging to SA and PVA. Magnetic hydrogels have demonstrated significant potential in the field of neural tissue engineering. These materials can respond to external magnetic field, which facilitates the favorable growth of cells on the hydrogel matrix.[49,50] In a recent study, we reported that magnetic coatings of SA/PVA/MNPs containing aligned MNPs were rougher, decreasing the proliferation of HT-22 neural cells.[51] Magnetic SA/PVA hydrogels were also successfully applied for Fenton degradation of organic dyes.[52]

In this study, SA/PVA compositions both in the absence and presence of MNPs at concentrations of 1.0 mg/mL, 2.5 mg/mL, and 5.0 mg/mL were subjected to 3D printing and subsequently crosslinked using Ca^{2+} ions via post-spraying. The rheological properties of the precursor gels were assessed since they have an impact on printability.[53] The 3D printed scaffolds were characterized using standard techniques such as scanning electron microscopy (SEM), gel content analysis, swelling degree determination. Additionally, the magnetic properties of the 3D printed scaffolds were evaluated through vibrating-sample magnetometry (VSM) and magnetic force microscopy (MFM). The mechanical properties of the 3D printed scaffolds were measured in their swollen state using nanoindentation with an atomic force microscope and colloidal probe.[30] The size and shape of the colloidal probe can be accurately determined, minimizing the uncertainty in the determination of the elastic modulus. We consider this to be a significant contribution because there is limited information available in the existing literature regarding the nanomechanical properties of swollen 3D printed scaffolds and the changes in the stiffness of the scaffolds due to the addition of MNPs. Employing the HT-22 cell lineage to assess the 3D printed scaffolds provides a relevant and accessible model to investigate the scaffolds' compatibility, potential neuronal effects, and the influence of magnetic nanoparticles.

2. RESULTS AND DISCUSSION

Detailed information regarding the experimental procedure for the preparation, 3D printing, statistical

analysis, and characterization of magnetic nanoparticles (MNPs), hydrogels, and 3D printed scaffolds can be found in the **Supporting Information**.

2.1 Rheological behavior and printability of the hydrogels. Viscosity is a key parameter for a successful 3D printing.[53] Particularly, the extrusion process enables printing inks or hydrogels with a wide range of viscosity; however, very low viscosity systems might generate structures that lose their shape after printing, and high viscosity systems might be difficult to print.[54] The viscosity of the hydrogels can be tuned by changing the polymer concentration or molecular weight or by combining two polymers or polymer and nanoparticles. Furthermore, non-Newtonian fluids with shear-thinning behavior have shown to be more adequate for bioprinting.[53]

The SA20 (SA 20wt%), SA16/PVA4 (SA/PVA 16/4 wt%), and SA12/PVA8 (SA/PVA 12/8 wt%) solutions presented shear-thinning behavior in the shear rate ($\dot{\gamma}$) range from 0.2 s^{-1} to 20 s^{-1} (**Figure 1a**). The viscosity curves were fitted to the Carreau model (**Table S1**), yielding viscosity values at zero shear rate (η_0) for SA20, SA16/PVA4, and SA12/PVA8 of 790 Pa.s, 584 Pa.s, and 270 Pa.s, respectively. SA20, SA16/PVA4, and SA12/PVA8 solutions seem to have the required flow properties to be successfully applied in the 3D printing, but preliminary tests indicated that SA12/PVA8 had the best printability because it had the lowest (η_0) values, requiring less pressure to print. Consequently, the magnetic SA/PVA-MNP1 (MNP 1.0 mg mL^{-1}), SA/PVA-MNP2.5 (2.5 mg mL^{-1}), and SA/PVA-MNP5 (MNP 5.0 mg mL^{-1}) hydrogels were prepared at the SA12/PVA8 composition. The SA/PVA-MNP1, SA/PVA-MNP2.5 and SA/PVA-MNP5 dispersions also presented shear-thinning behavior at moderate shear rates (0.2 s^{-1} to 20 s^{-1}) (**Figure 1b**). The η_0 values determined from the Carreau model fittings (**Table S1**) decreased from 270 Pa.s (SA12/PVA8) to 226 Pa.s (SA/PVA-MNP1), 165 Pa.s (SA/PVA-MNP2.5), and 103 Pa.s (SA/PVA-MNP5).

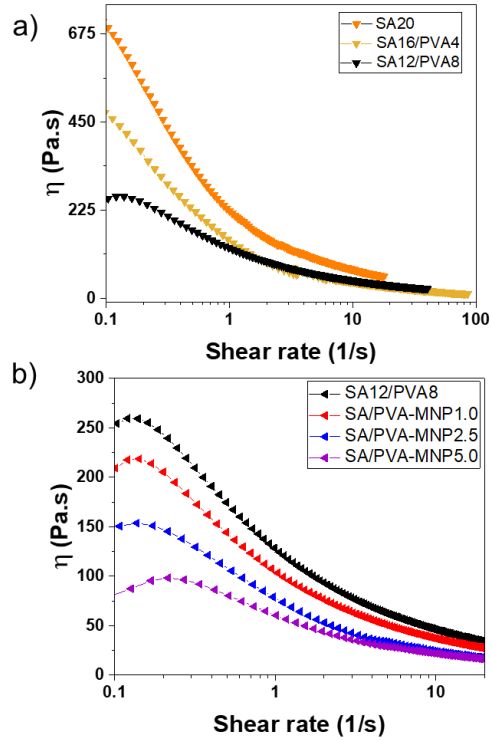

Figure 1. Viscosity (η) as a function of shear rate ($\dot{\gamma}$) for aqueous (**a**) solutions of SA20, SA16/PVA4, and SA12/PVA8, and (**b**) SA12/PVA8 solution, and SA/PVA-MNP1.0, SA/PVA-MNP2.5, and SA/PVA-MNP5.0 dispersions at 23 °C.

The miscibility between SA and PVA is mainly driven by hydrogen bonding between SA and PVA hydroxyl groups and ion-dipole interaction between the SA carboxylate groups and PVA hydroxyl groups (**Scheme 1a**). MNPs are physically entrapped in the three-dimensional network by hydrogen bonds[49] among the hydroxyl groups present on their surface (Fe-OH groups) and those belonging to PVA and SA (**Scheme 1b**). Thus, the number of available hydroxyl groups to keep the intermolecular interactions between SA and PVA decreases, decreasing the intermolecular friction. Also, the increase of MNP content can cause the increase of clusters size of magnetic particles due to magnetic attraction,[55,56] resulting in fewer junction points. These factors provide a potential explanation for the observed decrease in viscosity of the polymer-MNP solutions.

Figure 2a shows sweep frequency oscillatory curves determined at 23 °C in the strain range of 0.001 and 10 and frequency of 1 Hz for SA12/PVA8 solution, and SA/PVA-MNP1.0, SA/PVA-MNP2.5, and SA/PVA-MNP5.0 dispersions before crosslinking with Ca^{2+} ions. All systems presented G" > G', indicating liquid-like behavior, and the G" plateau values followed the same

trend observed for the η_o values, namely, SA12/PVA8 ≈ SA/PVA-MNP1.0 > SA/PVA-MNP2.5 > SA/PVA-MNP5.0. After crosslinkings with Ca^{2+} ions, all systems presented G' > G" (**Figures 2b-2e**), indicating solid-like behavior, for strain values less than 0.05 and evidencing the crosslinking process. Ca2+ ions can interact not only with SA carboxylate groups but also with PVA hydroxyl groups through ion-dipole interactions, as depicted in **Scheme 1c**. The disruption of intermolecular interactions and ionic bonds at strain range > 0.05 led to a decrease in the storage modulus, diminishing the solid-like behavior of the matrices. The flow points (τ_{flow}) extracted from G'/G" crossover (**Figure 2f**) decreased with the increase of MNP content, indicating that the MNPs compete for the carboxylic acid groups belonging to SA, remaining less coordination points for the Ca^{2+} ions (**Schemes 1c** and **1d**).

Calcium ions (Ca^{2+}) were used to crosslink the printed hydrogels. The crosslinking occurs due to the electrostatic interaction between the carboxylate groups (COO^-) present in the SA G-blocks and the positively charged calcium ions, forming the "egg box junctions" [57]. PVA chains are entrapped in the SA network and stabilized by hydrogen bonds between hydroxyl groups stemming from PVA and SA [58].

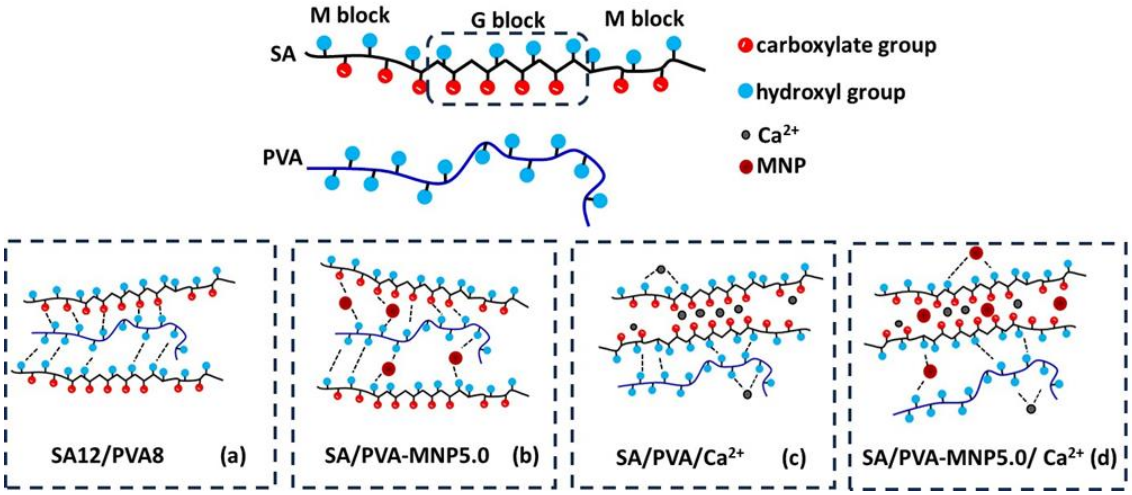

Scheme1. Representation of SA and PVA chains, carboxylate (red sphere) and hydroxyl (blue spheres) groups, MNPs (brown spheres), and Ca^{2+} ions (gray spheres). (a) SA12/PVA8 solution, (**b**) SA/PVA-MNP5.0 dispersion, (**c**) SA12/PVA8 solution in the presence of Ca^{2+} ions, and (d) SA/PVA-MNP5.0 dispersion in the presence of Ca^{2+} ions. The dot lines represent possible H bonding or ion-dipole interactions.

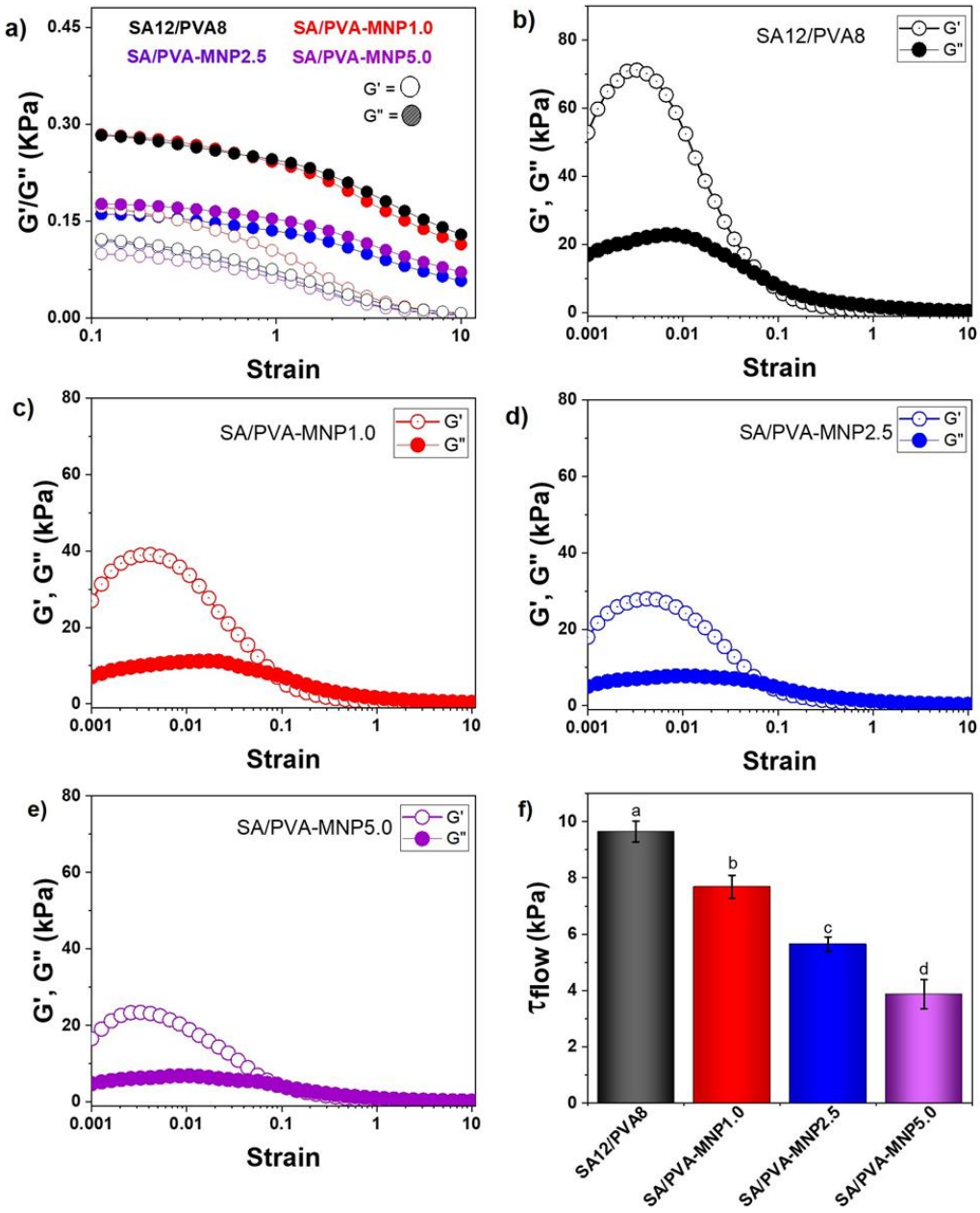

Figure 2. Strain sweep curves obtained at 1 Hz for (**a**) SA12/PVA8, SA/PVA-MNP1, SA/PVA-MNP2.5, and SA/PVA-MNP5 before cross-linking and (**b**) SA12/PVA8, (c) SA/PVA-MNP1.0, (d) SA/PVA-MNP2.5, and (**e**) SA/PVA-MNP.05 after cross-linking with Ca^{2+} ions. (**f**) Flow points (τ_{flow}) extracted from G'/G" crossover of each system after crosslinking. The different letters mean that the values are statistically different ($p < 0.05$).

The solution expansion after ink extrusion and the filament fusion with the previous extruded layers are factors that can cause the loss of resolution after printing.[48] SA12/PVA8, SA/PVA-MNP1.0, SA/PVA-MNP2.5, and SA/PVA-MNP5.0 presented good printability and the resolution was adequate due to the fast crosslinking of the SA chains mediated by the Ca^{2+} ions. The crosslinking with Ca^{2+} ions was performed by spraying the Ca^{2+} ions solution (3 wt%) either after each layer deposition (**Figure 3a, picture I**) or only after finishing the whole printing process (**Figure 3a, picture II**). The former process led to more uniform mesh resolution (angular intersection = 90°), for this reason it was kept for the crosslinking of the printed magnetic hydrogels. In the case of the magnetic hydrogels, the printing pressure and speed and flow rate were reduced to improve the filaments formation (**Table S2**) and minimize needle clogging by magnetic cluster. [59,60]

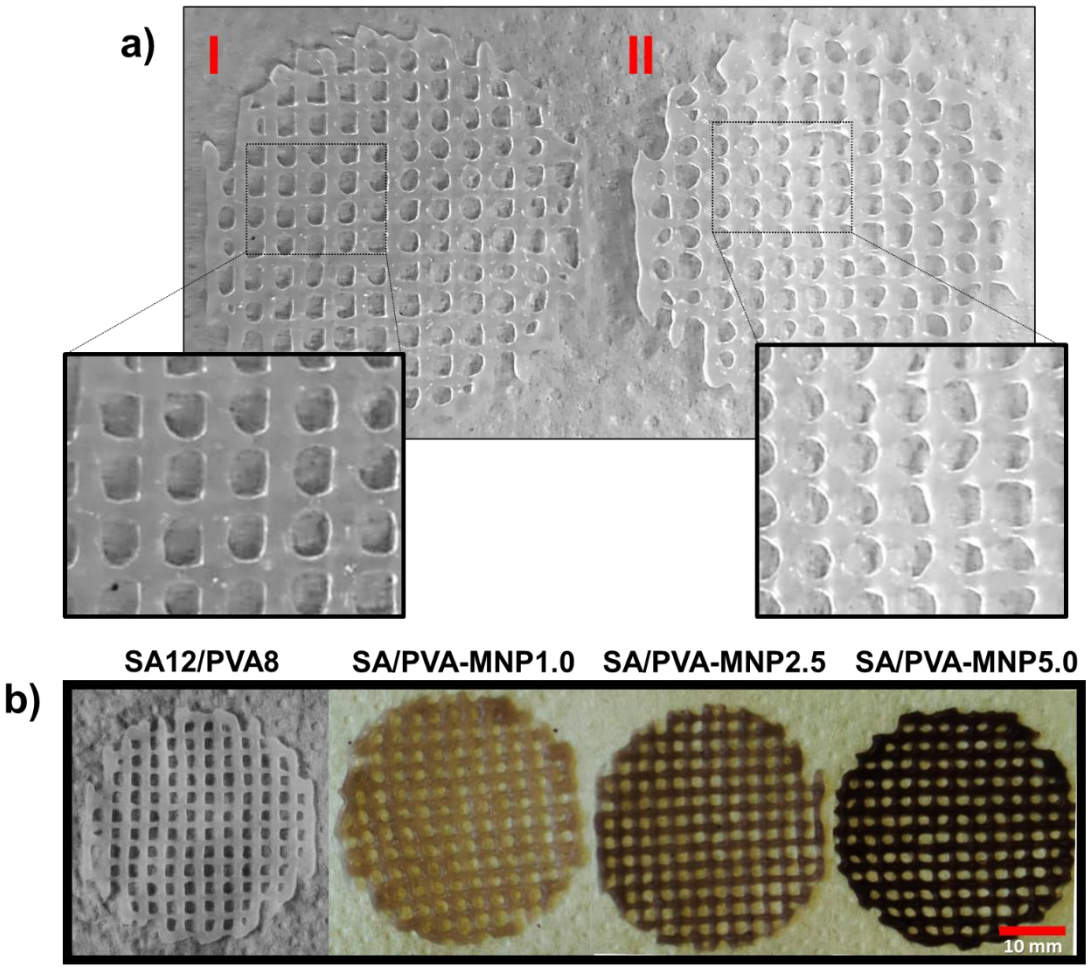

Figure 3. (**a**) Printed SA/PVA hydrogels (40 mm diameter, 3 mm of distance between the filaments). The crosslinking with Ca^{2+} ions was performed by spraying the Ca^{2+} ions solution (3 wt%) either after each layer deposition (**I**) or only after finishing the whole printing process (**II**). In both cases, additionally, the samples were immersed into a calcium ions solution (3 wt%) for 30 min. (**b**) Printed SA12/PVA8 and SA/PVA- MNP1.0, SA/PVA-MNP2.5, and SA/PVA-MNP5.0 hydrogels (40 mm diameter, 3 mm of distance between the filaments) obtained by process (**I**), the scale bar corresponds to 10 mm. Approximately 7 mL of each dispersion was extruded uninterruptedly.

2.2 Characterization of the freeze-dried crosslinked printed scaffolds. **Figure 4** shows the SEM images obtained for the SA12/PVA8, SA/PVA-MNP1.0, SA/PVA-MNP2.5, and SA/PVA-MNP5.0 scaffolds. All surfaces presented macropores and fine crosslinked fibers. Their formation was probably induced by the extrusion process because no fine fibers were observed for SA12/PVA8 films prepared by casting, crosslinking by spraying the Ca^{2+} ions solution (3 wt%) and freeze-drying (**Figure S1**). As the concentration of MNPs increased, the fibrils became less frequent and the macropores appeared larger. This effect might be attributed to a decrease in the available crosslinking sites, specifically carboxyl groups, which are essential for the formation of a dense and well-structured fibrous network. The MNPs might compete for the binding sites (**Scheme 1d**), resulting in less fibrils. Therefore, the incorporation of MNPs in the printing solution can have a significant impact on the morphology, mechanical and functional properties of the

printed scaffolds. The contribution of the gold sputtered layer was disregarded due to the formation of gold islands typically measuring 20 nm.[61] These islands are significantly larger than the observed structures.

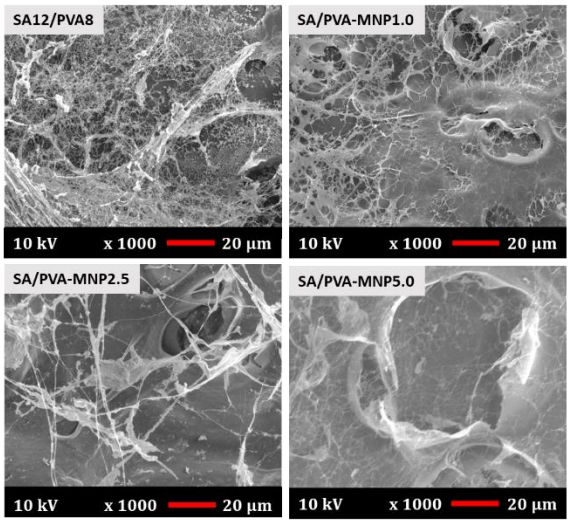

Figure 4. SEM images obtained for the SA12/PVA8, SA/PVA-MNP1.0, SA/PVA-MNP2.5, and SA/PVA-MNP5.0 3D printed scaffolds.

The FTIR-ATR spectra of PVA and SA presented some characteristic bands at similar wavenumbers because they have common functional groups (**Figure S2**). The bands were attributed to the vibrational modes of the corresponding chemical bond: [62,63] 3400–3100 cm^{-1} (νO-H), 1590 cm^{-1} (νCOO_{asym}), 1415 cm^{-1} (νCOO_{sym}),1080 cm^{-1} (νC-O), 1025 cm^{-1} (νC-O-C) and 945 cm^{-1} attributed C-O vibrations of SA glycosidic bonds, respectively. The spectrum of PVA (powder) presented bands at 2912 cm^{-1} ($\nu_{as}CH_2$), 2834 cm^{-1}, ($\nu_{s}CH_2$), 1426 cm^{-1} , ($\delta_{s}CH_2$), and 1715 cm^{-1} (ν C=O) from the non-hydrolyzed acetate groups. In comparison to pure SA and PVA no significant shift of bands could be observed in the FTIR-ATR spectra of SA12/PVA8, SA/PVA- MNP1.0, SA/PVA-MNP2.5, and SA/PVA-MNP5.0 3D printed scaffolds (**Figure S2**).

Figure 5a shows the swelling degree (SD) values determined for the SA12/PVA8, SA/PVA-MNP1, SA/PVA-MNP2.5, and SA/PVA-MNP5 scaffolds in MilliQ® water at 23 °C, for 24 h, 36 h, 60 h, and 120 h. The SD values of SA12/PVA8 and SA/PVA-MNP1.0 were similar ($p > 0.05$); they increased from ~ 230 ± 20% (24 h) to 280 ± 20% (120 h), indicating that the low MNP content did not affect the SD values. The SD values determined for SA/PVA-MNP2.5 showed no significant variation ($p > 0.05$), measuring 291 ± 21% at 24 h and 316 ± 22% 120 h. These samples kept their integrity over the 120 h. On the other hand ($p > 0.05$), the SA/PVA-MNP5.0 samples presented the lowest SD values and became fragile after 36 h, respectively. As previously discussed, the increased concentration of MNPs led to diminished intermolecular interactions between SA and PVA.

In DMEM, the scaffolds displayed significantly higher SD values compared to those in water ($p < 0.05$), as shown in **Figure 5b** and evidenced by photographs in **Figure S3**. Moreover, these SD values exhibited a notable increase over time. DMEM (CaCl2 at 200 mg/L, NaCl at 6.4 g/L many amino acids, vitamins, other inorganic salts, bicarbonate, glucose, and phenol red) was not changed over time. The most remarkable swelling was observed for SA/PVA-MNP2.5, which presented SD value of 1958 ± 137% after 120 h. One plausible explanation for this phenomenon is a partial exchange of Ca^{2+} ions from the matrix with Na^{+} ions from the medium. This exchange could lead to a reduction in crosslinking, consequently increasing the water uptake of the scaffold. Czichy et al.[42] observed that when maintain methyl cellulose (MC)/SA/MNP scaffolds for 2 weeks at room temperature in a 0.9 wt% $CaCl_2$ solution, the scaffolds exhibited increased stiffness attribute to the diffusion of Ca^{2+} ions to the matrix. However, over the subsequent three weeks, the scaffolds transitioned to a more fragile state due to the release of MC (methyl cellulose) into the medium. Nevertheless, when immersed in a 0.9 wt% NaCl the MC/SA/MNPs scaffolds swelled so much that some of the samples decomposed.[42] It is worth noting that, despite an overall increase in difficulty in handling, the measurement of SD values for SA/PVA-MNP5.0 in DMEM proved impossible due to a loss of integrity in the samples. This observation aligns with rheological behavior, indicating diminished intermolecular interactions among PVA and SA chains, attributed to the elevated content of MNPs.

The gel content (%) values (**Figure 5c**) determined for the SA12/PVA8, SA/PVA-MNP1.0, SA/PVA-MNP2.5, and SA/PVA-MNP5.0 3D printed scaffolds after 1 d, 7 d and 14 days in PBS (pH 7.4) were statistically similar ($p > 0.05$), indicating that the presence of MNPs did not affect the crosslinking because they interact well with both polymers, promoting physical crosslinkings. The gel content of ~80% remained even after 14 days, which is considered a good level for hydrogels[64,65] and show their adequacy to be applied as scaffolds for cell culture.

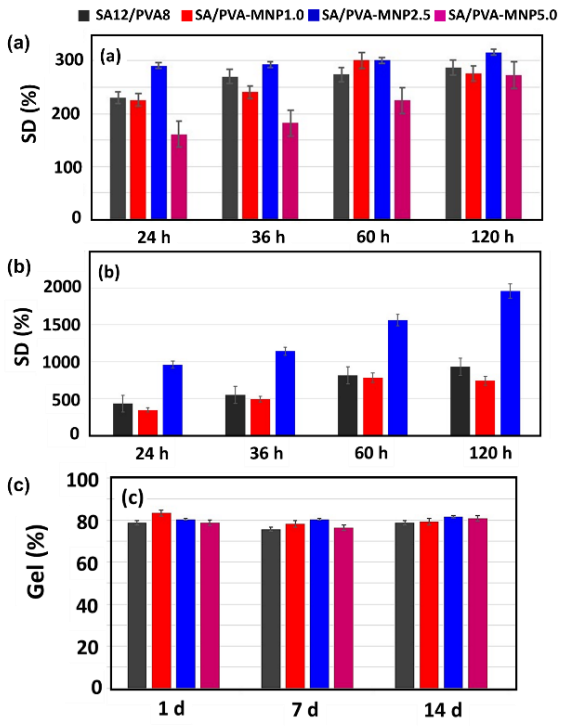

Figure 5. Swelling degree (SD) values in **(a)** MilliQ® water determined for the SA12/PVA8, SA/PVA-MNP1, SA/PVA-MNP2.5, and SA/PVA-MNP5 samples, and **(b)** DMEM determined for the SA12/PVA8, SA/PVA-MNP1, and SA/PVA-MNP2.5 printed scaffolds, after 24 h, 36 h, 60 h, and 120 h in the corresponding medium, at 23 °C. **(c)** Gel content (%) values determined for the SA12/PVA8, SA/PVA-MNP1.0, SA/PVA-MNP2.5, and SA/PVA-MNP5.0 3D printed scaffolds after 1 d, 7 d and 14 days in PBS (pH 7.4), at 23 °C.

The technique of magnetic force microscopy (MFM) offers distinct advantages for analyzing magnetic domains in composites.[66] MFM provides high-resolution imaging capabilities, enabling the visualization and characterization of magnetic domains at the nanoscale.[67] Moreover, MFM allows the direct mapping of magnetic properties, facilitating the understanding of domain formation, interactions, and dynamics within the composite material. On the SA/PVA-MNP1.0 scaffold (**Figure 6a**), the magnetic domains appeared distributed as small clusters (red regions), which were associated with the highest regions (white and light brown regions) observed in the corresponding topographic image. Similarly, on the SA/PVA-MNP2.5 sample (**Figure 6b**) the clusters of MNP were randomly distributed (red regions), and most magnetic regions were the highest in the topographic image. In contrast, on the SA/PVA-MNP5.0 scaffold (**Figure 6c**) the magnetic signal (red region) was observed on larger spots, indicating the presence of larger MNP clusters due to the aggregation of the MNPs.

The magnetization data obtained using the VSM technique for the SA/PVA-MNP1.0, SA/PVA-MNP2.5, and SA/PVA-MNP5.0 scaffolds revealed distinct trends. Pure MNPs exhibited a magnetization saturation (σ_s) of 63.6 emu/g and a coercivity (H_c) of 35 Oe (**Figure S4**). The magnetization curve determined for SA/PVA-MNP1 (**Figure 6a**) displayed a significantly lower σ_s of 0.46 emu/g, which corresponded to 0.70 wt% of MNP (calculation with **eq. 4** and **Figure S5** provided in the **Supporting Information**). The SA/PVA-MNP2.5 and SA/PVA-MNP5 scaffolds (**Figure 6b** and **6c**) presented σ_s values of 0.69 emu/g and 2.51 emu/g, corresponding to 1.1 wt% and 3.9 wt% of MNP. For comparison, magnetic scaffolds of poly(ε-caprolactone) (PCL) containing MNPs at 5wt% and 10 wt% presented magnetization of 1.6 emu/g and 3.1 emu/g, respectively.[68] These results indicated a positive correlation between the concentration of magnetic nanoparticles and the measured properties, highlighting the potential of these hydrogels for biomedical applications requiring sufficient magnetization levels [69–72].

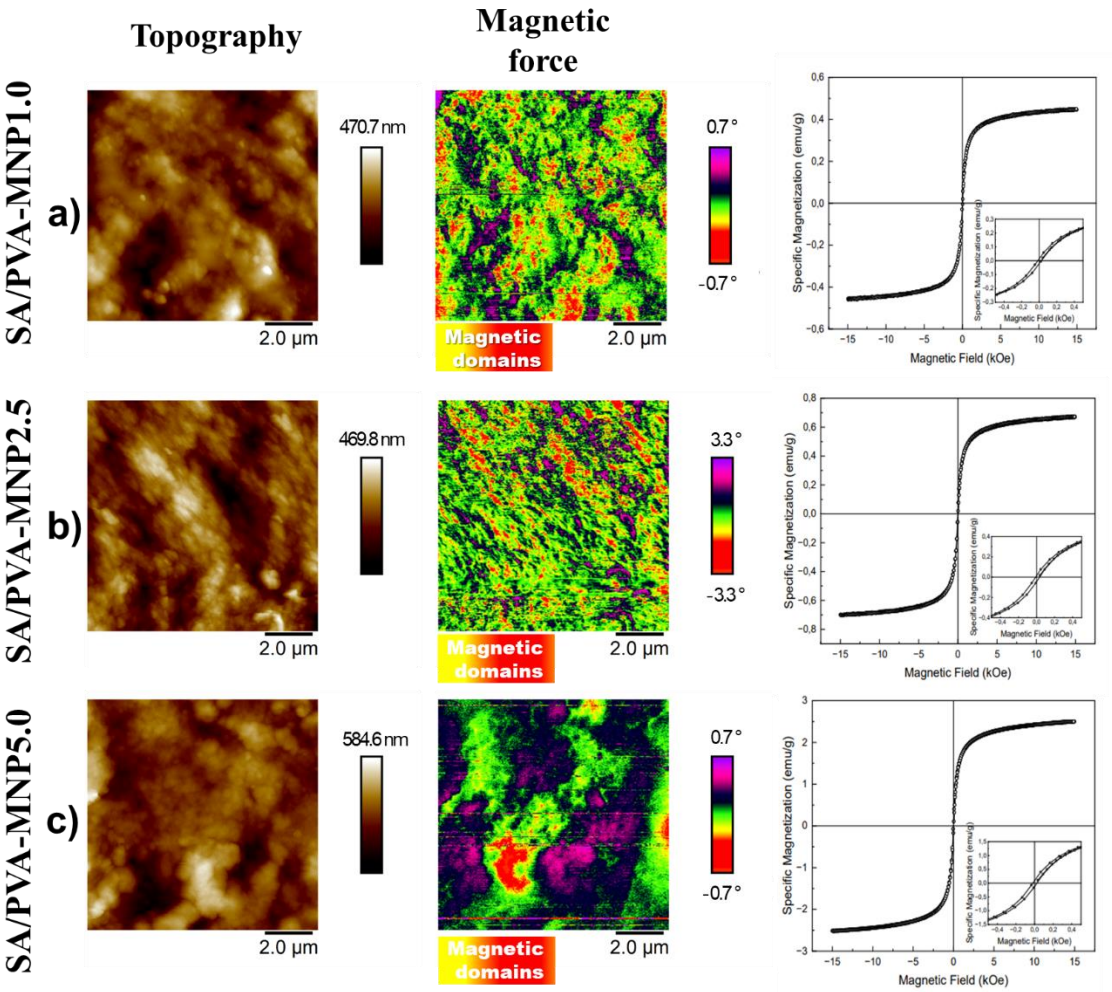

Figure 6. AFM (topography), MFM (magnetic force) and magnetization curves (hysteresis loops) obtained for (**a**) SA/PVA-MNP1.0, (**b**) SA/PVA-MNP2.5, and (**c**) SA/PVA-MNP5.0 scaffolds.

There is limited available information regarding the nanomechanical properties of (i) swollen printed scaffolds and (ii) the alterations in the stiffness of the scaffolds resulting from the presence of MNPs. Some reports indicate that the addition of MNPs turn the scaffolds stiffer. For instance, magnetic poly(ε-caprolactone) (PCL) samples were cast and freeze-dried; the Young's modulus (E) values determined by dynamic mechanical analysis for wet PCL scaffolds increased from 1.2 MPa to 1.4 MPa and 2.4 MPa, 5wt% and 10 wt% of MNPs were added[68]. Electrospun PCL fibers containing MNPs (0, 5 or 7 wt/v%) were analyzed using uniaxial tensile testing for samples swollen in PBS at 37 °C; the magnetic PCL samples were stiffer than pure PCL fibers due to the alignment of the MNPs.[73] Copper and silver particles filled PLA nanocomposites prepared via fused filament fabrication (FFF) additive manufacturing; the incorporation of bronze particles into the neat PLA increases the elastic modulus up to 10% and 27% for samples printed in 0° and 90° configurations, respectively, whereas the stiffness increased up to 103% for silver filled PLA nanocomposite scaffolds.[74] 3D printed hybrid magnetorheological silicon based elastomers were softer than the pure elastomer when no external magnetic field was applied, but under a magnetic field they presented higher stiffness compared to that of the pure elastomer.[75]

Other studies indicate that the addition of MNPs led to softer materials or had no effect on the stiffness. For example, the addition of 20 wt% of iron-doped hydroxyapatite (FeHA) to 3D printed PCL matrix led to softer scaffolds.[76] The reduced elastic modulus (Er) and contact hardness (Hc) values determined by nanoindentation of dry hydroxyapatite (HA)/magnetite (90/10 wt %) or pure HA porous scaffolds after 4- and 12-weeks implantation were similar and amounted to ~ 17 GPa and ~0.7 GPa, respectively,

indicating no significant effect of magnetite content on the mechanical properties.[77] The indentation of bacterial cellulose (BC) membranes in distilled water using a Berkovich indenter indicated E values ranging from 2.5 MPa to 40 MPa; their magnetic counterparts were softer.[78]

Figure 7a shows typical force-distance (FD) curves determined for swollen (in distilled water) SA12/PVA8, SA/PVA-MNP1.0, SA/PVA-MNP2.5, and SA/PVA-MNP5.0 scaffolds. The FD curves performed in PBS were not reliable because the phosphate groups interacted with the Ca^{2+} ions, reducing the scaffold integrity.

Figure 7b shows the indentation of the probe on the surface of each sample, with a maximum load of 800 nN. The indentation on the SA/PVA hydrogel exhibited a softer surface, typically characteristic of viscoelastic polymers [79]. As the content of MNPs increased in the composition, the surface becomes stiffer, resulting in smaller indentation depths. The Young's modulus (E) values were estimated with the Sneddon model (Eq. 4), and the values extracted from the FD curves. In average 400 FD curves were analyzed for each sample. **Figures 7c-7f** show the distribution of the E values over 400 FD curves determined for SA12/PVA8, SA/PVA-MNP1.0, SA/PVA-MNP2.5, and SA/PVA-MNP5.0, respectively; the range of E values and the corresponding standard deviations (sd) ranged from 0.18-6.70 MPa (sd = 0.89 MPa), 0.22-38.61 MPa (sd = 5.11 MPa), 0.06-49.54 MPa (sd = 5.84 MPa), and 0.45-58.25 MPa (sd = 10.51 MPa), respectively. The broad range of E values might be due to the sample heterogeneity and surface roughness. Particularly, for the magnetic samples, the MFM images clearly showed the random distribution of the MNPs on the surface (**Figure 6**), making them rough and irregular (**Figure S6**). The surface roughness can lead to erroneous interpretation of the distance between the average surfaces because the first contact with any irregularity is taken as zero distance.[30]

Surface irregularities cause variability in the E values, as depicted in **Figure 7g**. Thus, the study of E's variability is facilitated by using defined intervals (quartiles). The median value of the elastic modulus (Q2) for SA12/PVA8 was 0.6 MPa, and the introduction of MNPs led to an increase in this value from 2.0 MPa to 2.9 MPa, respectively. The interquartile range (IQR) remained relatively consistent for both the SA12/PVA8 and SA/PVA-MNP1 samples, measuring at 1.2 MPa and 1.3 MPa, respectively. However, for SA/PVA-MNP2.5 and SA/PVA-MNP5, the range extended to 2.6 MPa and 7.4 MPa, respectively. Notably, the presence of outliers also exhibited a gradual increase in this context. The statistical analysis of the mean E of the samples (Tukey's range test) showed that there is no significant difference between SA/PVA-MNP1.0 and SA/PVA-MNP2.5 ($p > 0.05$), but SA12/PVA8 is statistically different for the magnetic samples ($p < 0.05$).

Given that the MNPs are dispersed within the polymer matrix, it is important to note that the AFM FD curves are influenced from the surroundings.[79] Considering the specific conditions of these samples, it is reasonable to expect that the E would demonstrate an increase as the depth of indentation goes deeper. The analysis using MFM also unveiled expanding groups of MNP clusters. Consequently, it is anticipated that these clusters may introduce interference in the indentation measurements, as illustrated in **Figure 7h**. Furthermore, the chances of the probe to indent regions with multiple contacts increases, thereby complicating the deduction of the elastic modulus within this region.[79]

The E values range estimated for swollen scaffolds makes them adequate to be applied as scaffolds for cell culture. Dry SA based cryogels presented soft macroscopic mechanical strength (E = 0.01-5 kPa), but remarkably high local stiffness (E = 117 MPa), as assessed through AFM nanoindentation in the air [80]. These cryogels were successfully applied as scaffolds for human neuroblastoma-derived cell lines (SH-SY5Y), fostering the development of a greater number of neurites with highly branched morphologies compared to the control group, which utilized PLO/laminin coating.[80]

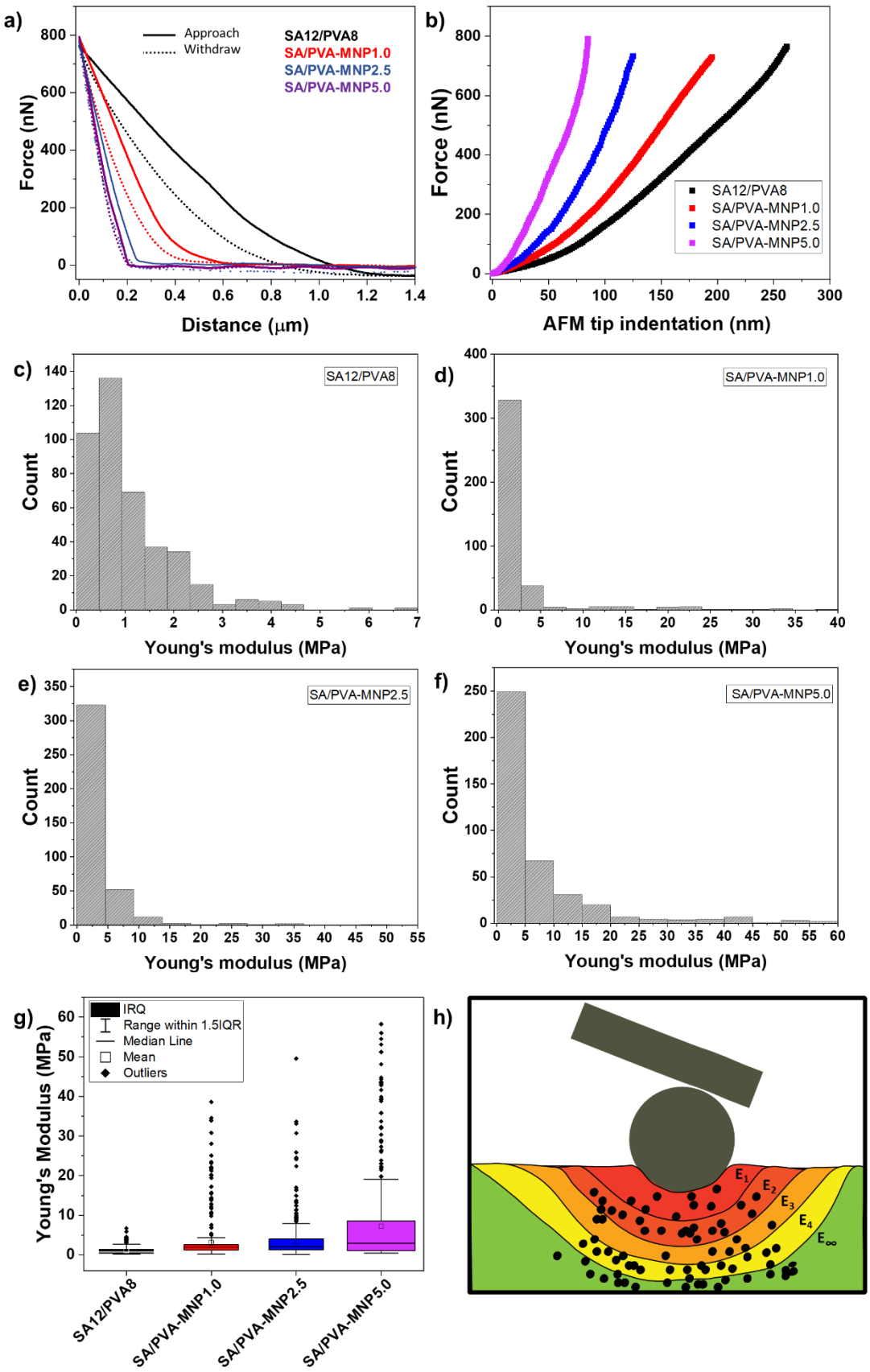
a)
Approach
Withdraw
SA12/PVA8
SA/PVA-MNP1.0
SA/PVA-MNP2.5
SA/PVA-MNP5.0
Force (nN)
Distance (μm)
b)
Force (nN)
AFM tip indentation (nm)
SA12/PVA8
SA/PVA-MNP1.0
SA/PVA-MNP2.5
SA/PVA-MNP5.0
c)
SA12/PVA8
Count
Young's modulus (MPa)
d)
SA/PVA-MNP1.0
Count
Young's modulus (MPa)
e)
SA/PVA-MNP2.5
Count
Young's modulus (MPa)
f)
SA/PVA-MNP5.0
Count
Young's modulus (MPa)
g)
IRQ
Range within 1.5IQR
Median Line
Mean
Outliers
Young's Modulus (MPa)
SA12/PVA8
SA/PVA-MNP1.0
SA/PVA-MNP2.5
SA/PVA-MNP5.0
h)
E1
E2
E3
E4
E∞

Figure 7. (**a**) Typical approach and retract curves, and (**b**) typical nanoindentation curves obtained with colloidal probe on 3D printed SA12/PVA8, SA/PVA-MNP1.0, SA/PVA-MNP2.5, and SA/PVA-MNP5.0 scaffolds. Histogram of Young's modulus (E) estimated from the slopes of nanoindentation curves (n = 400) within the linear elastic range for (**c**) SA12/PVA8, (**d**) SA/PVA-MNP1.0, (**e**) SA/PVA-MNP2.5, and (**f**) SA/PVA-MNP5.0 scaffolds. (**g**) Descriptive analysis for the Young's modulus values (E) for each sample. (**h**) Schematic representation of the E mapping in surfaces these composites as a function of the indentation depth. Black dots represent the clustering of MNPs embedded in the hydrogel.

2.3 Cell viability assays. The cell viability of the 3D printed SA12/PVA8, SA/PVA/MNP1.0, SA/PVA/MNP2.5, and SA/PVA/MNP5.0 samples was assessed using the MTS viability assay. This assay was conducted following the guidelines outlined in ISO 10993-5:2009 for the HT-22 cell line, which is derived from mouse hippocampal tissue. Remarkably, all tested samples, namely SA/PVA, SA/PVA/MNP1.0, SA/PVA/MNP2.5, and SA/PVA/MNP5.0, exhibited cell viability above 100% compared to the control (cultured on plastic plate). This indicates a favorable environment for cellular growth and proliferation (**Figure 8**). Although no statistically significant difference was found among the samples ($p > 0.05$), the SA/PVA/MNP2.5 scaffold exhibited the highest cell viability at 120%, suggesting its potential for enhanced neural cell adhesion and proliferation. These promising results pave the way for further investigations into the neurobiological applications of these magnetic hydrogel composites, such as neural tissue engineering and drug delivery systems, which can benefit from the cytocompatibility and magnetic properties offered by the synthesized materials.

Another conclusion that can be drawn is that the HT-22 cells appeared to behave similarly on the swollen scaffolds, which had elastic modulus values in the range of ~ 1 MPa to ~ 7 MPa. In other words, this range of elastic modulus is likely suitable for this type of cell, and any stiffening resulting from the presence of the MNPs was not noticeable.

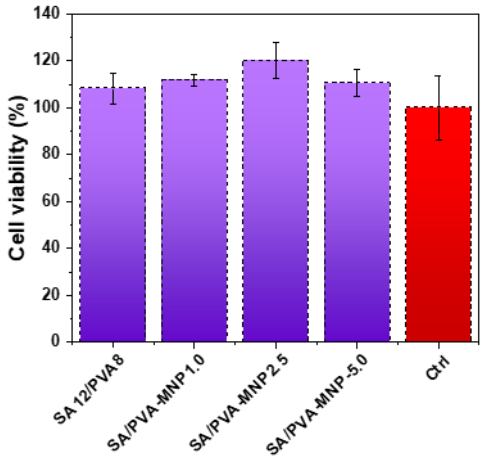

Figure 8. MTS viability assays (24 h) performed for HT-22 cells with extracting solutions from 3D printed SA12/PVA8, SA/PVA/MNP1, SA/PVA/MNP2.5, and SA/PVA/MNP5 scaffolds. The control (Ctrl) refers to the cells grown on the commercial culture plate.

The morphology of HT-22 cells was evaluated after 48 h culturing on the 3D printed SA/PVA-MNP2.5 scaffolds. F**igure 9a shows** a typical optical micrography **o**f the SA/PVA-MNP2.5 scaffold containing adhered species (bright regions), possibly organized as cell clusters. DAPI- and anti-F-actin-labeled cells were observed using confocal fluorescence microscopy. **Figure 9b** displays clusters of cells on the hydrogel; their cytoskeleton appeared red due to the phalloidin 633 dye, while the nucleus appeared blue due to the Hoechst 33342 dye. The rounded and compact cell shape observed here has been reported in other publications involving adherent cells and 3D scaffolds. This phenomenon could be attributed to factors such as small pore size, chemical composition, or mechanical properties that influence cell self-organization.[81,82] In **Figure 9c**, the plasticity of the cells is evident as they spread in depth, reaching approximately 80 µm in height. This indicates that the matrix provides suitable conditions for three-dimensional proliferation. Similar

entities were observed throughout the sample, suggesting cell diffusion within the scaffold (as seen in the z-stack in Figure **9c**).

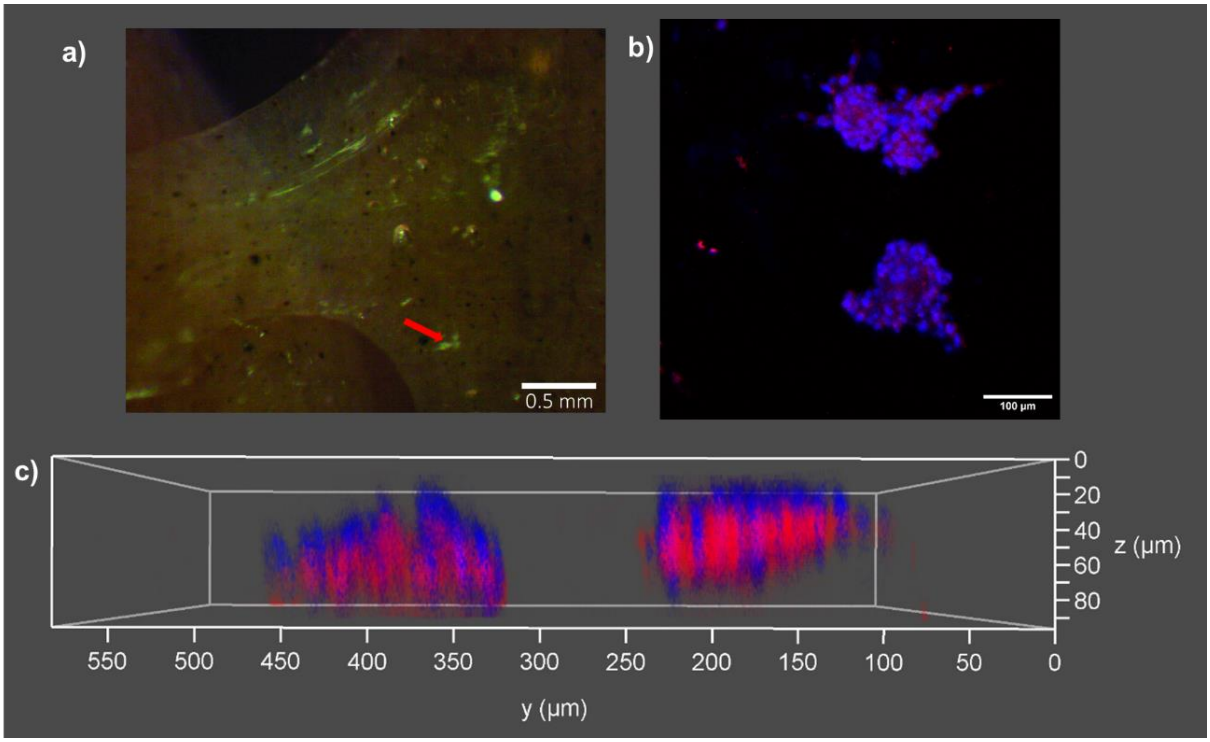

Figure 9. Images of HT-22 cells adhered to the surface and in the interior of SA/PVA-MNP2.5 scaffolds. (**a**) Optical microscopy, the red arrow points to cell clusters. (**b**) and (**c**) Confocal microscopy, showing nuclei and f-actin of cells stained with Hoechst 33342 and phalloidin 633 dyes, respectively.

3. CONCLUSIONS

In this research, we developed scaffolds by compounding SA12/Alg8 and MPNs at 1.0, 2.5, and 5.0 mg/ml. These compositions exhibited suitable 3D printability and could be readily crosslinked with Ca^{2+} ions. Increasing the MNP content in the 3D scaffolds, several notable changes were observed: the surface displayed fewer fibrils and more macropores, the swelling degree decreased, magnetization increased, and larger magnetic clusters appeared more frequently, as revealed by MFM. Nanoindentation using AFM to assess the nanomechanical properties of the magnetic scaffolds indicated that the swollen hydrogels became stiffer as more MNPs were incorporated into the scaffolds. Importantly, these 3D printed scaffolds did not display any cytotoxicity when tested with HT-22 cells. These findings are particularly relevant because while magnetic composites have found extensive use in biomedical applications, there is limited information available in the existing literature concerning the nanomechanical properties of swollen 3D printed scaffolds and the impact of MNP addition on scaffold stiffness. Additionally, the combination of MFM and nanoindentation provides valuable insights into the microenvironment that cells experience during *in vitro* cell culture assays. Anticipating upcoming studies, which encompass *in vitro* examinations of genetic material and in vivo assays, we posit that these interconnected hydrogels hold considerable potential for diverse applications. The magnetic hydrogel's responsiveness to external magnetic fields can trigger various actions, including the release of bioactive species entrapped in or the modification of its surface properties. Moreover, these hydrogels can serve as platforms for creating artificial environments suitable to cell studies or drug testing under magnetic stimuli.

ASSOCIATED CONTENT

The **Supporting Information** is available free of charge at XXXX

Experimental details of synthesis and characterization of magnetic nanoparticles (MNPs); X-ray diffrac-

togram and magnetic hysteresis of bare MNPs; preparation of the hydrogels and 3D printing conditions; rheological parameters for the characterization of the hydrogels and magnetic dispersions; instrumental details used for each technique used for the characterization of the freeze-dried crosslinked printed scaffolds; cell viability and imaging; X-ray diffractogram and magnetic hysteresis of bare MNPs; printing parameters and digital photographs of the printed scaffolds captured from a lateral perspective; fitting parameters using Carreau's model; SEM image of freeze-dried 3D printed and cast SA12/PVA8 hydrogel; FTIR-ATR spectra; photographs of the swollen scaffolds, and cross-sections of the AFM topographic images.

AUTHORS INFORMATION

Corresponding Authors

Amin Shavandi: Université Libre de Bruxelles (ULB), Ecole polytechnique de Bruxelles, 3BIO-BioMatter, Avenue F.D. Roosevelt, 50—CP 165/61, 1050, Brussels, Belgium; ORCID: 0000-0002-0188-3090; Email: amin.shavandi@ulb.be

Denise F. Petri: Department of Fundamental Chemistry, Institute of Chemistry, University of São Paulo, Av. Prof. Lineu Prestes 748, 05508-000, São Paulo, Brazil; ORCID: 0000-0003-4814-8357; Email: dfsp@iq.usp.br

Authors

Alex C. Alavarse: Department of Fundamental Chemistry, Institute of Chemistry, University of São Paulo, Av. Prof. Lineu Prestes 748, 05508-000, São Paulo, Brazil; ORCID 0000-0003-2866-1305.

Rafael L. C. G. da Silva: Department of Fundamental Chemistry, Institute of Chemistry, University of São Paulo, Av. Prof. Lineu Prestes 748, 05508-000, São Paulo, Brazil; ORCID 0000-0002-2114-3815.

Pejman Ghaffari Bohlouli: Université Libre de Bruxelles (ULB), Ecole polytechnique de Bruxelles, 3BIO-BioMatter, Avenue F.D. Roosevelt, 50—CP 165/61, 1050, Brussels, Belgium. ORCID 0000-0002-0188-3090.

Daniel Cornejo: Institute of Physics, University of São Paulo, 05508-090 São Paulo, Brazil. ORCID 0000-0003-1133-2599.

Henning Ulrich: Department of Biochemistry, Institute of Chemistry, University of São Paulo, Av. Prof. Lineu Prestes 748, 05508-000, São Paulo, Brazil. ORCID 0000-0002-2114-3815.

AUTHOR CONTRIBUTIONS

The manuscript was written through contributions of all authors.

FUNDING SOURCES

This work was supported by the Conselho Nacional de Desenvolvimento Científico e Tecnológico (CNPq Grant **304017/2021-3, 406396/2021 and 308012/2021-6**) and São Paulo Research Foundation (FAPESP, grants **2018/13492-2**, **2019/22671-0**, **2020/01907-3**, **2022/08442-1** and **2018/07366–4**). A. S. acknowledges financial support from FNRS-Fonds de la Recherche Scientifique for projets bilatéraux de mobilité (PINT-BILAT-M) R. **M014.19** (**35704283**).

ACKNOWLEDGMENT

The authors express their gratitude to Ms. Julia Simińska-Stanny for providing training on the use of the 3D printer.

REFERENCES

(1) Advincula, R. C.; Dizon, J. R. C.; Caldona, E. B.; Viers, R. A.; Siacor, F. D. C.; Maalihan, R. D.; Espera, A. H. On the Progress of 3D-Printed Hydrogels for Tissue Engineering. *MRS Commun.* **2021**, *11* (5), 539–553. https://doi.org/10.1557/S43579-021-00069-1/TABLES/2.

(2) Zhu, Y.; Joralmon, D.; Shan, W.; Chen, Y.; Rong, J.; Zhao, H.; Xiao, S.; Li, X. 3D Printing Biomimetic Materials and Structures for Biomedical Applications. *Bio-Design Manuf. 2021 42* **2021**, *4* (2), 405–428. https://doi.org/10.1007/S42242-020-00117-0.

(3) Zamboulis, A.; Michailidou, G.; Koumentakou, I.; Bikiaris, D. N. Polysaccharide 3D Printing for Drug Delivery Applications. *Pharm. 2022, Vol. 14, Page 145* **2022**, *14* (1), 145. https://doi.org/10.3390/PHARMACEUTICS14010145.

(4) Zhang, M.; Qiao, X.; Han, W.; Jiang, T.; Liu, F.; Zhao, X. Alginate-Chitosan Oligosaccharide-ZnO Composite Hydrogel for Accelerating Wound Healing. *Carbohydr. Polym.* **2021**, *266*, 118100. https://doi.org/10.1016/J.CARBPOL.2021.118100.

(5) Gao, L.; Zhou, Y.; Peng, J.; Xu, C.; Xu, Q.; Xing, M.; Chang, J. A Novel Dual-Adhesive and Bioactive Hydrogel Activated by Bioglass for Wound Healing. *NPG Asia Mater.* **2019**, *11* (1), 66.

https://doi.org/10.1038/s41427-019-0168-0.

(6) You, J.; Xie, S.; Cao, J.; Ge, H.; Xu, M.; Zhang, L.; Zhou, J. Quaternized Chitosan/Poly(Acrylic Acid) Polyelectrolyte Complex Hydrogels with Tough, Self-Recovery, and Tunable Mechanical Properties. *Macromolecules* **2016**, *49* (3), 1049–1059. https://doi.org/10.1021/acs.macromol.5b02231.

(7) Riahi, N.; Liberelle, B.; Henry, O.; De Crescenzo, G. Impact of RGD Amount in Dextran-Based Hydrogels for Cell Delivery. *Carbohydr. Polym.* **2017**, *161*, 219–227. https://doi.org/https://doi.org/10.1016/j.carbpol.2017.01.002.

(8) Alavarse, A. C.; Frachini, E. C. G.; Silva, J. B.; Pereira, R. dos S.; Ulrich, H.; Petri, D. F. S. Amino Acid Decorated Xanthan Gum Coatings: Molecular Arrangement and Cell Adhesion. *Carbohydr. Polym. Technol. Appl.* **2022**, *4*, 100227. https://doi.org/10.1016/J.CARPTA.2022.100227.

(9) Hadrich, A.; Dulong, V.; Rihouey, C.; Labat, B.; Picton, L.; Le Cerf, D. Biomimetic Hydrogel by Enzymatic Crosslinking of Pullulan Grafted with Ferulic Acid. *Carbohydr. Polym.* **2020**, *250*, 116967. https://doi.org/https://doi.org/10.1016/j.carbpol.2020.116967.

(10) Kim, Y.; Zhao, X. Magnetic Soft Materials and Robots. *Chem. Rev.* **2022**, *122* (5), 5317–5364. https://doi.org/10.1021/acs.chemrev.1c00481.

(11) Zhalmuratova, D.; Chung, H.-J. Reinforced Gels and Elastomers for Biomedical and Soft Robotics Applications. *ACS Appl. Polym. Mater.* **2020**, *2* (3), 1073–1091. https://doi.org/10.1021/acsapm.9b01078.

(12) Ceylan, H.; Yasa, I. C.; Yasa, O.; Tabak, A. F.; Giltinan, J.; Sitti, M. 3D-Printed Biodegradable Microswimmer for Theranostic Cargo Delivery and Release. *ACS Nano* **2019**, *13* (3), 3353–3362. https://doi.org/10.1021/acsnano.8b09233.

(13) Yasa, I. C.; Tabak, A. F.; Yasa, O.; Ceylan, H.; Sitti, M. 3D-Printed Microrobotic Transporters with Recapitulated Stem Cell Niche for Programmable and Active Cell Delivery. *Adv. Funct. Mater.* **2019**, *29* (17), 1808992. https://doi.org/https://doi.org/10.1002/adfm.201808992.

(14) Lin, H.-Y.; Huang, H.-Y.; Shiue, S.-J.; Cheng, J.-K. Osteogenic Effects of Inductive Coupling Magnetism from Magnetic 3D Printed Hydrogel Scaffold. *J. Magn. Magn. Mater.* **2020**, *504*, 166680. https://doi.org/https://doi.org/10.1016/j.jmmm.2020.166680.

(15) Huang, Z.; He, Y.; Chang, X.; Liu, J.; Yu, L.; Wu, Y.; Li, Y.; Tian, J.; Kang, L.; Wu, D.; Wang, H.; Wu, Z.; Qiu, G. A Magnetic Iron Oxide/Polydopamine Coating Can Improve Osteogenesis of 3D-Printed Porous Titanium Scaffolds with a Static Magnetic Field by Upregulating the TGFβ-Smads Pathway. *Adv. Healthc. Mater.* **2020**, *9* (14), 2000318. https://doi.org/https://doi.org/10.1002/adhm.202000318.

(16) Podstawczyk, D.; Nizioł, M.; Szymczyk, P.; Wiśniewski, P.; Guiseppi-Elie, A. 3D Printed Stimuli-Responsive Magnetic Nanoparticle Embedded Alginate-Methylcellulose Hydrogel Actuators. *Addit. Manuf.* **2020**, *34*, 101275. https://doi.org/https://doi.org/10.1016/j.addma.2020.101275.

(17) Zhang, J.; Zhao, S.; Zhu, M.; Zhu, Y.; Zhang, Y.; Liu, Z.; Zhang, C. 3D-Printed Magnetic Fe3O4/MBG/PCL Composite Scaffolds with Multifunctionality of Bone Regeneration, Local Anticancer Drug Delivery and Hyperthermia. *J. Mater. Chem. B* **2014**, *2* (43), 7583–7595. https://doi.org/10.1039/C4TB01063A.

(18) Zhang, Y.; Zhai, D.; Xu, M.; Yao, Q.; Chang, J.; Wu, C. 3D-Printed Bioceramic Scaffolds with a Fe3O4/Graphene Oxide Nanocomposite Interface for Hyperthermia Therapy of Bone Tumor Cells. *J. Mater. Chem. B* **2016**, *4* (17), 2874–2886. https://doi.org/10.1039/C6TB00390G.

(19) Li, H.; Yin, Y.; Xiang, Y.; Liu, H.; Guo, R. A Novel 3D Printing PCL/GelMA Scaffold Containing USPIO for MRI-Guided Bile Duct Repair. *Biomed. Mater.* **2020**, *15* (4), 045004. https://doi.org/10.1088/1748-605X/ab797a.

(20) Paltanea, G.; Manescu (Paltanea), V.; Antoniac, I.; Antoniac, A.; Nemoianu, I. V; Robu, A.; Dura, H. A Review of Biomimetic and Biodegradable Magnetic Scaffolds for

Bone Tissue Engineering and Oncology. *International Journal of Molecular Sciences*. 2023. https://doi.org/10.3390/ijms24054312.

(21) Glaser, T.; Bueno, V. B.; Cornejo, D. R.; Petri, D. F. S.; Ulrich, H. Neuronal Adhesion, Proliferation and Differentiation of Embryonic Stem Cells on Hybrid Scaffolds Made of Xanthan and Magnetite Nanoparticles. *Biomed. Mater.* **2015**. https://doi.org/10.1088/1748-6041/10/4/045002.

(22) Singh, I.; Lacko, C. S.; Zhao, Z.; Schmidt, C. E.; Rinaldi, C. Preparation and Evaluation of Microfluidic Magnetic Alginate Microparticles for Magnetically Templated Hydrogels. *J. Colloid Interface Sci.* **2020**, *561*, 647–658. https://doi.org/https://doi.org/10.1016/j.jcis.2019.11.040.

(23) Kasper, M.; Ellenbogen, B.; Hardy, R.; Cydis, M.; Mojica-Santiago, J.; Afridi, A.; Spearman, B. S.; Singh, I.; Kuliasha, C. A.; Atkinson, E.; Otto, K. J.; Judy, J. W.; Rinaldi-Ramos, C.; Schmidt, C. E. Development of a Magnetically Aligned Regenerative Tissue-Engineered Electronic Nerve Interface for Peripheral Nerve Applications. *Biomaterials* **2021**, *279*, 121212. https://doi.org/https://doi.org/10.1016/j.biomaterials.2021.121212.

(24) Mohammadalizadeh, M.; Dabirian, S.; Akrami, M.; Hesari, Z. SPION Based Magnetic PLGA Nanofibers for Neural Differentiation of Mesenchymal Stem Cells. *Nanotechnology* **2022**, *33* (37), 375101. https://doi.org/10.1088/1361-6528/AC7402.

(25) Zhang, J.; Wang, Y.; Shu, X.; Deng, H.; Wu, F.; He, J. Magnetic Chitosan Hydrogel Induces Neuronal Differentiation of Neural Stem Cells by Activating RAS-Dependent Signal Cascade. *Carbohydr. Polym.* **2023**, *314*, 120918. https://doi.org/https://doi.org/10.1016/j.carbpol.2023.120918.

(26) Marovič, N.; Ban, I.; Maver, U.; Maver, T. Magnetic Nanoparticles in 3D-Printed Scaffolds for Biomedical Applications. **2023**, *12* (1). https://doi.org/doi:10.1515/ntrev-2022-0570.

(27) Rehfeldt, F.; Engler, A. J.; Eckhardt, A.; Ahmed, F.; Discher, D. E. Cell Responses to the Mechanochemical Microenvironment—Implications for Regenerative Medicine and Drug Delivery. *Adv. Drug Deliv. Rev.* **2007**, *59* (13), 1329–1339. https://doi.org/https://doi.org/10.1016/j.addr.2007.08.007.

(28) Wang, L.; Wang, C.; Wu, S.; Fan, Y.; Li, X. Influence of the Mechanical Properties of Biomaterials on Degradability, Cell Behaviors and Signaling Pathways: Current Progress and Challenges. *Biomater. Sci.* **2020**, *8* (10), 2714–2733. https://doi.org/10.1039/D0BM00269K.

(29) Islam, M. S.; Molley, T. G.; Hung, T.; Sathish, C. I.; Putra, V. D. L.; Jalandhra, G. K.; Ireland, J.; Li, Y.; Yi, J.; Kruzic, J. J.; Kilian, K. A. Magnetic Nanofibrous Hydrogels for Dynamic Control of Stem Cell Differentiation. *ACS Appl. Mater. Interfaces* **2023**, *15* (44), 50663–50678. https://doi.org/10.1021/acsami.3c07021.

(30) Butt, H.-J.; Cappella, B.; Kappl, M. Force Measurements with the Atomic Force Microscope: Technique, Interpretation and Applications. *Surf. Sci. Rep.* **2005**, *59* (1), 1–152. https://doi.org/https://doi.org/10.1016/j.surfrep.2005.08.003.

(31) Rettler, E.; Hoeppener, S.; Sigusch, B. W.; Schubert, U. S. Mapping the Mechanical Properties of Biomaterials on Different Length Scales: Depth-Sensing Indentation and AFM Based Nanoindentation. *J. Mater. Chem. B* **2013**, *1* (22), 2789–2806. https://doi.org/10.1039/C3TB20120A.

(32) Simič, R.; Mathis, C. H.; Spencer, N. D. A Two-Step Method for Rate-Dependent Nano-Indentation of Hydrogels. *Polymer (Guildf).* **2018**, *137*, 276–282. https://doi.org/https://doi.org/10.1016/j.polymer.2018.01.017.

(33) Zhang, S.; Weng, Y.; Ma, C. Quantitative Nanomechanical Mapping of Polyolefin Elastomer at Nanoscale with Atomic Force Microscopy. *Nanoscale Res. Lett.* **2021**, *16* (1), 113. https://doi.org/10.1186/s11671-021-03568-1.

(34) Magazzù, A.; Marcuello, C. Investigation of Soft Matter Nanomechanics by Atomic Force Microscopy and Optical Tweezers: A Comprehensive Review. *Nanomaterials*. 2023. https://doi.org/10.3390/nano13060963.

(35) Gheorghita Puscaselu, R.; Lobiuc, A.; Dimian, M.; Covasa, M. Alginate: From Food Industry to Biomedical Applications and Management of Metabolic Disorders. *Polymers*. 2020. https://doi.org/10.3390/polym12102417.

(36) Wu, Z.; Li, Q.; Xie, S.; Shan, X.; Cai, Z. In Vitro and in Vivo Biocompatibility Evaluation of a 3D Bioprinted Gelatin-Sodium Alginate/Rat Schwann-Cell Scaffold. *Mater. Sci. Eng. C* **2020**, *109*, 110530. https://doi.org/https://doi.org/10.1016/j.msec.2019.110530.

(37) Hu, C.; Lu, W.; Sun, C.; Zhao, Y.; Zhang, Y.; Fang, Y. Gelation Behavior and Mechanism of Alginate with Calcium: Dependence on Monovalent Counterions. *Carbohydr. Polym.* **2022**, *294*, 119788. https://doi.org/https://doi.org/10.1016/j.carbpol.2022.119788.

(38) Aranci, K.; Uzun, M.; Su, S.; Cesur, S.; Ulag, S.; Amin, A.; Guncu, M. M.; Aksu, B.; Kolayli, S.; Ustundag, C. B.; Silva, J. C.; Ficai, D.; Ficai, A.; Gunduz, O. 3D Propolis-Sodium Alginate Scaffolds: Influence on Structural Parameters, Release Mechanisms, Cell Cytotoxicity and Antibacterial Activity. *Molecules*. 2020. https://doi.org/10.3390/molecules25215082.

(39) Do, A.-V.; Akkouch, A.; Green, B.; Ozbolat, I.; Debabneh, A.; Geary, S.; Salem, A. K. Controlled and Sequential Delivery of Fluorophores from 3D Printed Alginate-PLGA Tubes. *Ann. Biomed. Eng.* **2017**, *45* (1), 297–305. https://doi.org/10.1007/s10439-016-1648-9.

(40) Li, P.; Cao, L.; Sang, F.; Zhang, B.; Meng, Z.; Pan, L.; Hao, J.; Yang, X.; Ma, Z.; Shi, C. Polyvinyl Alcohol/Sodium Alginate Composite Sponge with 3D Ordered/Disordered Porous Structure for Rapidly Controlling Noncompressible Hemorrhage. *Biomater. Adv.* **2022**, *134*, 112698. https://doi.org/https://doi.org/10.1016/j.msec.2022.112698.

(41) Janarthanan, G.; Lee, S.; Noh, I. 3D Printing of Bioinspired Alginate-Albumin Based Instant Gel Ink with Electroconductivity and Its Expansion to Direct Four-Axis Printing of Hollow Porous Tubular Constructs without Supporting Materials. *Adv. Funct. Mater.* **2021**, *31* (45), 2104441. https://doi.org/https://doi.org/10.1002/adfm.202104441.

(42) Czichy, C.; Spangenberg, J.; Günther, S.; Gelinsky, M.; Odenbach, S. Determination of the Young's Modulus for Alginate-Based Hydrogel with Magnetite-Particles Depending on Storage Conditions and Particle Concentration. *J. Magn. Magn. Mater.* **2020**, *501*, 166395. https://doi.org/https://doi.org/10.1016/j.jmmm.2020.166395.

(43) Kim, B.-S.; Baez, C. E.; Atala, A. Biomaterials for Tissue Engineering. *World J. Urol.* **2000**, *18* (1), 2–9. https://doi.org/10.1007/s003450050002.

(44) Gao, T.; Yang, Z.; Chen, C.; Li, Y.; Fu, K.; Dai, J.; Hitz, E. M.; Xie, H.; Liu, B.; Song, J.; Yang, B.; Hu, L. Three-Dimensional Printed Thermal Regulation Textiles. *ACS Nano* **2017**, *11* (11), 11513–11520. https://doi.org/10.1021/acsnano.7b06295.

(45) Cataldi, A.; Rigotti, D.; Nguyen, V. D. H.; Pegoretti, A. Polyvinyl Alcohol Reinforced with Crystalline Nanocellulose for 3D Printing Application. *Mater. Today Commun.* **2018**, *15*, 236–244. https://doi.org/https://doi.org/10.1016/j.mtcomm.2018.02.007.

(46) He, H. Y.; Zhang, J. Y.; Mi, X.; Hu, Y.; Gu, X. Y. Rapid Prototyping for Tissue-Engineered Bone Scaffold by 3D Printing and Biocompatibility Study. *Int. J. Clin. Exp. Med.* **2015**, *8* (7), 11777.

(47) England, S.; Rajaram, A.; Schreyer, D. J.; Chen, X. Bioprinted Fibrin-Factor XIII-Hyaluronate Hydrogel Scaffolds with Encapsulated Schwann Cells and Their in Vitro Characterization for Use in Nerve Regeneration. *Bioprinting* **2017**, *5*, 1–9. https://doi.org/https://doi.org/10.1016/j.bprint.2016.12.001.

(48) Wei, Q.; Yang, R.; Sun, D.; Zhou, J.; Li, M.; Zhang, Y.; Wang, Y. Design and Evaluation of Sodium Alginate/Polyvinyl Alcohol Blend Hydrogel for 3D Bioprinting Cartilage Scaffold: Molecular Dynamics Simulation and Experimental Method. *J. Mater. Res. Technol.* **2022**, *17*, 66–78. https://doi.org/10.1016/J.JMRT.2021.12.130.

(49) Kondaveeti, S.; Semeano, A. T. S.; Cornejo, D. R.; Ulrich, H.; Petri, D. F. S. Magnetic Hydrogels for Levodopa Release and Cell

Stimulation Triggered by External Magnetic Field. *Colloids Surfaces B Biointerfaces* **2018**. https://doi.org/10.1016/j.colsurfb.2018.04.040.

(50) Plen, R.; Smith, A.; Blum, O.; Aloni, O.; Locker, U.; Shapira, Z.; Margel, S.; Shefi, O. Bioengineering 3D Neural Networks Using Magnetic Manipulations. *Adv. Funct. Mater.* **2022**, *32* (50), 2204925. https://doi.org/https://doi.org/10.1002/adfm.202204925.

(51) Alavarse, A. C.; Silva, J. B.; Ulrich, H.; Petri, D. F. S. Poly(Vinyl Alcohol)/Sodium Alginate/Magnetite Composites: Magnetic Force Microscopy for Tracking Magnetic Domains. *Soft Matter* **2023**, *19* (14), 2612–2622. https://doi.org/10.1039/D3SM00053B.

(52) Zhang, M.-K.; Ling, X.-H.; Zhang, X.-H.; Han, G.-Z. A Novel Alginate/PVA Hydrogel-Supported Fe3O4 Particles for Efficient Heterogeneous Fenton Degradation of Organic Dyes. *Colloids Surfaces A Physicochem. Eng. Asp.* **2022**, *652*, 129830. https://doi.org/https://doi.org/10.1016/j.colsurfa.2022.129830.

(53) Kyle, S.; Jessop, Z. M.; Al-Sabah, A.; Whitaker, I. S. 'Printability" of Candidate Biomaterials for Extrusion Based 3D Printing: State-of-the-Art.' *Adv. Healthc. Mater.* **2017**, *6* (16), 1700264. https://doi.org/https://doi.org/10.1002/adhm.201700264.

(54) Mirzaei, M.; Okoro, O. V.; Nie, L.; Petri, D. F. S.; Shavandi, A. Protein-Based 3D Biofabrication of Biomaterials. *Bioeng. 2021, Vol. 8, Page 48* **2021**, *8* (4), 48. https://doi.org/10.3390/BIOENGINEERING8040048.

(55) Appel, E. A.; Tibbitt, M. W.; Webber, M. J.; Mattix, B. A.; Veiseh, O.; Langer, R. Self-Assembled Hydrogels Utilizing Polymer–Nanoparticle Interactions. *Nat. Commun. 2015 61* **2015**, *6* (1), 1–9. https://doi.org/10.1038/ncomms7295.

(56) Zhang, S.; Gao, H.; Guo, P.; Li, T.; Lin, T.; Ding, R.; Wang, Z.; He, P. Fabrication and Extrusion of the PAAm-SAlg Hydrogels with Magnetic Particles. *Colloids Surfaces A Physicochem. Eng. Asp.* **2020**, *603*, 125280. https://doi.org/10.1016/J.COLSURFA.2020.125280.

(57) Cao, L.; Lu, W.; Mata, A.; Nishinari, K.; Fang, Y. Egg-Box Model-Based Gelation of Alginate and Pectin: A Review. *Carbohydr. Polym.* **2020**, *242*, 116389. https://doi.org/https://doi.org/10.1016/j.carbpol.2020.116389.

(58) Safi, S.; Morshed, M.; Hosseini Ravandi, S. A.; Ghiaci, M. Study of Electrospinning of Sodium Alginate, Blended Solutions of Sodium Alginate/Poly(Vinyl Alcohol) and Sodium Alginate/Poly(Ethylene Oxide). *J. Appl. Polym. Sci.* **2007**, *104* (5), 3245–3255. https://doi.org/https://doi.org/10.1002/app.25696.

(59) Kania, A.; Berent, K.; Mazur, T.; Sikora, M. 3D Printed Composites with Uniform Distribution of Fe3O4 Nanoparticles and Magnetic Shape Anisotropy. *Addit. Manuf.* **2021**, *46*, 102149. https://doi.org/10.1016/J.ADDMA.2021.102149.

(60) Yunus, D. E.; Sohrabi, S.; He, R.; Shi, W.; Liu, Y. Acoustic Patterning for 3D Embedded Electrically Conductive Wire in Stereolithography. *J. Micromechanics Microengineering* **2017**, *27* (4), 045016. https://doi.org/10.1088/1361-6439/AA62B7.

(61) Siqueira Petri, D. F.; Wenz, G.; Schunk, P.; Schimmel, T. An Improved Method for the Assembly of Amino-Terminated Monolayers on SiO2 and the Vapor Deposition of Gold Layers. *Langmuir* **1999**, *15* (13), 4520–4523. https://doi.org/10.1021/la981379u.

(62) Silverstein, R. M.; Bassler, G. C.; Morrill, T. Chapter Three: Infrared Spectrometry. *Spectrom. Identif. Org. Compd. Fifth Ed.* **1991**, 91–164.

(63) Prabha, G.; Raj, V. Sodium Alginate–Polyvinyl Alcohol–Bovin Serum Albumin Coated Fe3O4 Nanoparticles as Anticancer Drug Delivery Vehicle: Doxorubicin Loading and in Vitro Release Study and Cytotoxicity to HepG2 and Lo2 Cells. *Mater. Sci. Eng. C* **2017**, *79*, 410–422. https://doi.org/https://doi.org/10.1016/j.msec.2017.04.075.

(64) García-Astrain, C.; Avérous, L. Synthesis and Behavior of Click Cross-Linked Alginate Hydrogels: Effect of Cross-Linker Length and Functionality. *Int. J. Biol. Macromol.* **2019**, *137*, 612–619. https://doi.org/10.1016/J.IJBIOMAC.2019.0

7.010.

(65) Spoljaric, S.; Salminen, A.; Luong, N. D.; Seppälä, J. Stable, Self-Healing Hydrogels from Nanofibrillated Cellulose, Poly(Vinyl Alcohol) and Borax via Reversible Cross-linking. *Eur. Polym. J.* **2014**, *56* (1), 105–117. https://doi.org/10.1016/J.EURPOLYMJ.2014.03.009.

(66) Winkler, R.; Ciria, M.; Ahmad, M.; Plank, H.; Marcuello, C. A Review of the Current State of Magnetic Force Microscopy to Unravel the Magnetic Properties of Nanomaterials Applied in Biological Systems and Future Directions for Quantum Technologies. *Nanomaterials*. 2023. https://doi.org/10.3390/nano13182585.

(67) Kazakova, O.; Puttock, R.; Barton, C.; Corte-León, H.; Jaafar, M.; Neu, V.; Asenjo, A. Frontiers of Magnetic Force Microscopy. *J. Appl. Phys.* **2019**, *125* (6), 060901. https://doi.org/10.1063/1.5050712.

(68) Kim, J. J.; Singh, R. K.; Seo, S. J.; Kim, T. H.; Kim, J. H.; Lee, E. J.; Kim, H. W. Magnetic Scaffolds of Polycaprolactone with Functionalized Magnetite Nanoparticles: Physicochemical, Mechanical, and Biological Properties Effective for Bone Regeneration. *RSC Adv.* **2014**. https://doi.org/10.1039/c4ra00040d.

(69) Wang, Z.; Zhu, H.; Li, H.; Wang, Z.; Sun, M.; Yang, B.; Wang, Y.; Wang, L.; Xu, L. High-Strength Magnetic Hydrogels with Photoweldability Made by Stepwise Assembly of Magnetic-Nanoparticle-Integrated Aramid Nanofiber Composites. *ACS Nano* **2023**, *17* (10), 9622–9632. https://doi.org/10.1021/acsnano.3c03156.

(70) Boztepe, C.; Daskin, M.; Erdogan, A. Synthesis of Magnetic Responsive Poly(NIPAAm-Co-VSA)/Fe3O4 IPN Ferrogels and Modeling Their Deswelling and Heating Behaviors under AMF by Using Artificial Neural Networks. *React. Funct. Polym.* **2022**, *173*, 105219. https://doi.org/https://doi.org/10.1016/j.reactfunctpolym.2022.105219.

(71) Shuai, C.; Cheng, Y.; Yang, W.; Feng, P.; Yang, Y.; He, C.; Qi, F.; Peng, S. Magnetically Actuated Bone Scaffold: Microstructure, Cell Response and Osteogenesis. *Compos. Part B Eng.* **2020**, *192*, 107986. https://doi.org/10.1016/J.COMPOSITESB.2020.107986.

(72) Singh, R.; Pal, D.; Chattopadhyay, S. Target-Specific Superparamagnetic Hydrogel with Excellent PH Sensitivity and Reversibility: A Promising Platform for Biomedical Applications. *ACS Omega* **2020**, *5* (34), 21768–21780. https://doi.org/10.1021/acsomega.0c02817.

(73) Leal-Marin, S.; Gallaway, G.; Höltje, K.; Lopera-Sepulveda, A.; Glasmacher, B.; Gryshkov, O. Scaffolds with Magnetic Nanoparticles for Tissue Stimulation. **2021**, *7* (2), 460–463. https://doi.org/doi:10.1515/cdbme-2021-2117.

(74) Alam, F.; Shukla, V. R.; Varadarajan, K. M.; Kumar, S. Microarchitected 3D Printed Polylactic Acid (PLA) Nanocomposite Scaffolds for Biomedical Applications. *J. Mech. Behav. Biomed. Mater.* **2020**, *103*, 103576. https://doi.org/https://doi.org/10.1016/j.jmbbm.2019.103576.

(75) Bastola, A. K.; Hoang, V. T.; Li, L. A Novel Hybrid Magnetorheological Elastomer Developed by 3D Printing. *Mater. Des.* **2017**, *114*, 391–397. https://doi.org/https://doi.org/10.1016/j.matdes.2016.11.006.

(76) De Santis, Roberto and Russo, Alessandro and Gloria, Antonio and D'Amora, Ugo and Russo, Teresa and Panseri, Silvia and Sandri, Monica and Tampieri, Anna and Marcacci, Maurilio and Dediu, Valentin A. and Wilde, Colin J. and Ambrosio, L. Towards the Design of 3D Fiber-Deposited Poly(-Caprolactone)/Iron-Doped Hydroxyapatite Nanocomposite Magnetic Scaffolds for Bone Regeneration. *J. Biomed. Nanotechnol.* **2015**, *11* (7), 1236–1246. https://doi.org/10.1166/jbn.2015.2065.

(77) Russo, A.; Bianchi, M.; Sartori, M.; Boi, M.; Giavaresi, G.; Salter, D. M.; Jelic, M.; Maltarello, M. C.; Ortolani, A.; Sprio, S.; Fini, M.; Tampieri, A.; Marcacci, M. Bone Regeneration in a Rabbit Critical Femoral Defect by Means of Magnetic Hydroxyapatite Macroporous Scaffolds. *J. Biomed. Mater. Res. Part B Appl. Biomater.* **2018**, *106* (2), 546–554. https://doi.org/https://doi.org/10.1002/jbm.b.33836.

(78) Pavón, J. J.; Allain, J. P.; Verma, D.; Echeverry-Rendón, M.; Cooper, C. L.; Reece, L. M.; Shetty, A. R.; Tomar, V. In Situ Study

Unravels Bio-Nanomechanical Behavior in a Magnetic Bacterial Nano-Cellulose (MBNC) Hydrogel for Neuro-Endovascular Reconstruction. *Macromol. Biosci.* **2019**, *19* (2), 1800225. https://doi.org/https://doi.org/10.1002/mabi.201800225.

(79) Collinson, D. W.; Sheridan, R. J.; Palmeri, M. J.; Brinson, L. C. Best Practices and Recommendations for Accurate Nanomechanical Characterization of Heterogeneous Polymer Systems with Atomic Force Microscopy. *Prog. Polym. Sci.* **2021**, *119*, 101420. https://doi.org/https://doi.org/10.1016/j.progpolymsci.2021.101420.

(80) Béduer, A.; Braschler, T.; Peric, O.; Fantner, G. E.; Mosser, S.; Fraering, P. C.; Benchérif, S.; Mooney, D. J.; Renaud, P. A Compressible Scaffold for Minimally Invasive Delivery of Large Intact Neuronal Networks. *Adv. Healthc. Mater.* **2015**, *4* (2), 301–312. https://doi.org/https://doi.org/10.1002/adhm.201400250.

(81) Foraida, Z. I.; Kamaldinov, T.; Nelson, D. A.; Larsen, M.; Castracane, J. Elastin-PLGA Hybrid Electrospun Nanofiber Scaffolds for Salivary Epithelial Cell Self-Organization and Polarization. *Acta Biomater.* **2017**, *62*, 116–127. https://doi.org/https://doi.org/10.1016/j.actbio.2017.08.009.

(82) Singh, D.; Wang, S.-B.; Xia, T.; Tainsh, L.; Ghiassi-Nejad, M.; Xu, T.; Peng, S.; Adelman, R. A.; Rizzolo, L. J. A Biodegradable Scaffold Enhances Differentiation of Embryonic Stem Cells into a Thick Sheet of Retinal Cells. *Biomaterials* **2018**, *154*, 158–168. https://doi.org/https://doi.org/10.1016/j.biomaterials.2017.10.052.